PROCEEDINGS A

rspa.royalsocietypublishing.org

Research

Article submitted to journal

Keywords:
Granular media, rolling friction, plasticity

Rolling resistance on sand

Keaton J. Burns[1], Neil J. Balmforth[2], and Ian J. Hewitt[3]

[1]Department of Physics, Massachusetts Institute of Technology, Cambridge, MA, 02139, U.S.
[2]Department of Mathematics, University of British Columbia, 1984 Mathematics Road, Vancouver, BC, V6T 1Z2, Canada
[3] Mathematical Institute, University of Oxford, OX2 6GG, U.K.

Experiments are conducted to measure the resistance experienced by cylindrical shells rolling over flat beds of granular media. Sand and glass spheres are used for the beds. The rolling cylinders are optically tracked in videos to provide position as a function of time; fits to these trajectories provide velocity and acceleration data. For glass spheres, the rolling resistance is noticably dependent on velocity, but to a degree that is too strong to be explained by air drag. For sand, the rolling resistance has a less pronounced dependence on velocity. The results are compared to a theoretical model based on Mohr-Coulomb rheology for a granular medium. The model idealizes the flow pattern underneath the rolling cylinder as a plastically deforming zone in front of a rigidly rotating plug attached to the cylinder, as proposed previously for cylinders rolling on perfectly cohesive plastic media. The leading-order, rate-independent rolling resistance observed experimentally is well reproduced by the model predictions.

THE ROYAL SOCIETY PUBLISHING

1. Introduction

It is commonly experienced that motion over loose sand is hindered by the response of the granular medium to applied loads. In particular, sandy surfaces often present substantial difficulties to wheeled vehicles [1], impacting the design of tires and robotic rovers [2,3]. The rolling of individual rocks may also play a key role in geophysical processes such as the formation of screes [4]. Although Coulomb provided detailed measurements of the resistance to rolling, Reynolds [5] gave the first quantatitive discussion of the origin of the phenomenon in terms of the deformation of the surface in rolling contact. The resulting friction experienced by rubber and metal surfaces is now understood to be a combination of Reynolds' deformation and surface adhesion [6,7]. For wheels travelling over sand, the problem is complicated further by the lack of a general theory of the deformation of a granular medium, the significant depth to which the wheels of a heavy vehicle will sink, and substantial sideways sand flow. Nevertheless, a rich vein of literature has built up on the resistance to wheels driven over sand (*e.g.* [1,3,8–15]).

In this work, we consider the rolling motion of a long and light cylinder over an initially static granular bed. In this limit, the contact area between the cylinder and the bed is small relative to the surface area of the cylinder, and the deformation of the granular surface is largely two-dimensional and both localized and superficial. This sets our work apart from much of the literature on rotating wheels and recent experiments on rolling spheres [16], where the problem is inherently three-dimensional and the weight of the object traversing the surface leads to significant sinking and compaction of the underlying granular material. Additional complications are thereby minimized and we might hope to gain better insight into the dynamics of granular deformation under a rolling object.

Our study begins with a series of experiments with the main goal of determining the resistance experienced by the rolling cylinders. A particular focus is to explore the dependence on the speed of rolling, which reflects the rate-dependent rheology of the granular material and bears on the relevance of recently proposed empirical friction laws [17] For the task, we use two types of granular medium: a coarse sand and glass spheres (ballotini). For both, the grain size is much smaller than the radii of the rolling cylinders.

We complement the experiments with a theoretical model based on Mohr-Coulomb plasticity theory for the granular bed. In the limit that the contact area is much smaller than the cylinder area, the stress field induced by the rolling cylinder can be constructed by asymptotic theory. This device, which was proposed by Spencer [18,19], has been used previously to model the rolling of cylinders over cohesive material [20,21], neglecting the effect of gravity. Much as in the calculation of the critical load supported by a foundation [22–24], however, the effect of gravity cannot be neglected for a non-cohesive granular medium with a free surface. Our perturbation analysis generalizes Spencer's perturbation theory for a cylinder rolling over such material.

A critical detail of the generalization is the flow pattern that must be adopted underneath the contact region between the sand and cylinder. For this task, we adopt a construct proposed by Collins [25,26] in which the deformation due to rolling consists of two parts: a zone of plastic deformation extending below and ahead of the forward section of the contact region, together with a plug that is rigidly attached to the cylinder below the rear section of the contact region. Collins' construction allows for contacts that are not necessarily small and has received some support from numerical computations [15], but was proposed for cohesive material neglecting gravity. The two-part structure of the flow pattern is, however, essential for a consistent description of the forces and torques acting on the cylinder, and is reminiscent of experiments and models of wheels rolling over sand [9–14].

The experimental apparatus, procedures, and dataset are described in § 2. In § 3, we outline the theoretical model to calculate rolling resistance. We compare the predictions of the model to our experimental results in § 4. The Appendices contain some additional theoretical results, exposing (and correcting) some issues with the Mohr-Coulomb predictions for the velocity field and free surface of the granular medium, and relating our analysis back to that of Collins [25].

Material	$d\,(\mathrm{mm})$	$\rho_s\,(\mathrm{g/cm^3})$	$\phi\,(\mathrm{deg})$
Aquarium sand	0.9 ± 0.15	1.59 ± 0.09	37.9 ± 1.3
Ballotini	1.0 ± 0.2	1.55 ± 0.07	24.9 ± 0.7

Table 1: Mean particle diameter d, apparent density ρ_s, and friction angle ϕ of the granular media used in the experiments [27].

Cylinder	$M\,(\mathrm{g})$	$D\,(\mathrm{cm})$	$b\,(\mathrm{cm})$	$L\,(\mathrm{cm})$	α	$\rho_c\,(\mathrm{g/cm^3})$
20	48.13	2.687	0.315	15.0	0.793	0.5658
21	72.06	3.343	0.360	15.0	0.807	0.5473
22	94.27	4.237	0.370	15.0	0.840	0.4457
23	113.56	4.857	0.385	15.0	0.854	0.4086
24	153.25	6.042	0.425	15.0	0.869	0.3563
25	246	7.288	0.560	15.0	0.858	0.3931
26	312	8.896	0.560	15.0	0.882	0.3346
27	754	21.94	0.500	16.2	0.955	0.1231
28	43.45	5.103	0.160	15.0	0.939	0.1416
29	34.84	5.094	0.145	15.0	0.944	0.1139
30	204	11.412	0.330	15.0	0.943	0.1329
31	656	11.445	0.950	15.0	0.847	0.4251
32	55.27	4.217	0.290	15.0	0.871	0.2638
36	79.50	9.559	0.155	15.0	0.968	0.0738
42	12.89	4.245	0.055	15.0	0.974	0.0607

Table 2: Reference number, mass M, outer diameter D, wall thickness b, length L, dimensionless moment of inertia α, and mean density ρ_c for the cylinders used in the experiments.

2. Experiments

(a) Apparatus and protocol

We constructed a channel using a high-density polyethylene board and wooden siderails to contain a bed of granular material, over which we rolled a variety of cylinders. The channel was approximately $244\,\mathrm{cm}$ in length, $31\,\mathrm{cm}$ in width, and $9\,\mathrm{cm}$ in depth. Two granular materials were used in our experiments: PetCo aquarium sand, and Potters Industries A-100 glass beads (ballotini). Both materials had mean grain sizes near $1\,\mathrm{mm}$, but the sand grains were much coarser than the nearly spherical ballotini, resulting in a substantially different friction angles between the materials. The material parameters are provided in Table 1, and were taken from Sauret et al. [27], who used the same materials.

The rollers were sections cut from cylindrical tubing, primarily PVC and other plastic pipes. The cylinders spanned from approximately 1 to $11\,\mathrm{cm}$ in radius, and 10 to $650\,\mathrm{g}$ in mass. Detailed measurements of the cylinders are listed in Table 2. The cylinders were sanded, cleaned, painted with high-visibility orange spray paint, and sanded again to give them consistent surface textures and appearances. A camera was mounted to the ceiling above the bed to record the cylinders' trajectories in colour at 60 frames per second with a resolution of 1080p.

To prepare the granular bed, we filled the channel with a granular material, and then loosely scraped off the top surface layer down to a depth set using the top of the side-rails. No effort was made to compact the bed any further. To reset the bed after a disturbance to the surface, we manually stirred the material throughout its depth, and repeated the leveling procedure. On the ballotini, the cylinders typically left large (several millimeter deep) tracks as they rolled, so the surface was reset between each run. On the sand, the cylinders left tracks that were barely

perceptible to the naked eye, but which could be highlighted by shadows cast when the surface was illuminated from a position just above it and off to one side. The shadows revealed small levees on either side of the track left by the cylinders and showed how the sand surface between had been smoothed over the scale of a grain. To speed up the data taking process, we therefore only reset the sand surface when a large disturbance occurred (*e.g.* a stray or dropped cylinder). Despite the lack of any substantial surface rearrangment by the cylinders on the sand, the rolling resistance was more sensitive: the resistance was noticeably different when rolling a cylinder over its previous track (an effect familiar from the rolling of spheres over rubber and metal [6]). To reduce this affect as much as possible, we began the experiments with sand using a bedding-in procedure described in §(c).

The cylinders were placed on a rigid inclined ramp at the top of the runway and rolled onto the surface of the granular bed. The initial velocity of the cylinders as they entered the bed was controlled by adjusting the starting position of the cylinders along the ramp. Trials were deemed unsuccessful if they came within a few centimeters of the channel sidewalls, which tended to occur more frequently for lighter cylinders and at higher initial velocities. We repeated rolls until we recorded three to five successful trials with the same experimental parameters.

(b) Data processing

The post-processing consisted of three stages. First, "image trajectories" indicating the image coordinates of the cylinders for each video frame were calculated. Second, the position markers were used to infer the camera's projection for the scene. Third, the "object trajectories" indicating the real-space positions of the cylinders over time were extracted by inverting the camera projection for the calculated image trajectories. For the latter, we refer to the tops of the side-rails to define a laboratory coordinate system, with X pointing along the channel, Y across it, and Z directed vertically upwards.

(i) Image trajectories

Each cylinder was painted bright orange so that pixel colour precisely differentiated them from the bed and any other object in the scene. The OpenCV 3.0 library [28] was used to extract individual frames from the videos and convert them to hue-saturation-value (HSV) colour space. To each frame, we applied a light (11 pixel) Gaussian blur and then computed the HSV color distance d of each of the pixels within the granular bed from a reference orange value of $(4, 205, 255)$. Using d, we constructed a "match value" m for each pixel as $m = \frac{1}{2}[1 - \tanh(\frac{d-100}{5})]$, and took the centroid of match field to define the image position of the cylinder for that frame. The combination of the Gaussian blur and the smoothed match statistic (as opposed to a binary threshold) dithers the edges of the cylinder, allowing for sub-pixel precision in the determination of the cylinder's image centroid. Figure 1 shows these processing stages for an example frame, and figure 2 displays the image trajectory resulting from processing the entire movie sequence in this fashion.

(ii) Camera calibration

To accurately determine the cylinder's position in the lab frame from its image coordinates, the camera projection was precisely characterized. We performed a standard calibration using routines from the OpenCV 3.0 library, which are based on a pinhole camera model with corrections for common modes of lens distortion. The image coordinates of any point in the 3D laboratory frame was then estimated by composing the pose transformation for that scene with the intrinsic camera projection using the OpenCV `projectPoints` routine. The difference between these estimated image coordinates and the measured image coordinates for the distance markers constitutes the reprojection error. Our calibration procedure typically yielded reprojection errors of about $3.0\,\mathrm{px}$.

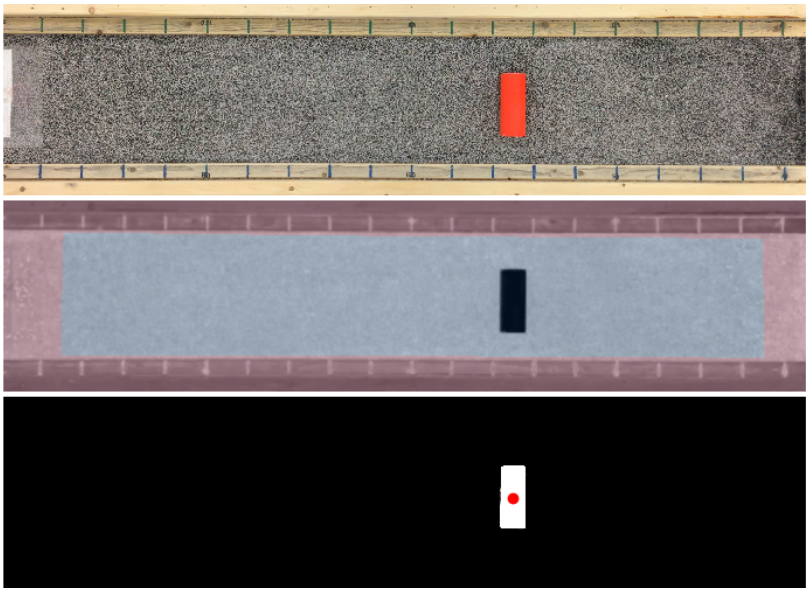

Figure 1: Stages of image-position extraction. Top: A frame from a video recording. Middle: Color distance from reference orange, indicated in greyscale with darker pixels being closer in HSV space. The shaded red region is excluded from further processing to isolate objects on the bed. Bottom: Match field derived from the color distance, with lighter pixels indicating a better match. The red dot indicates the centroid of the match field and defines the cylinder's image position.

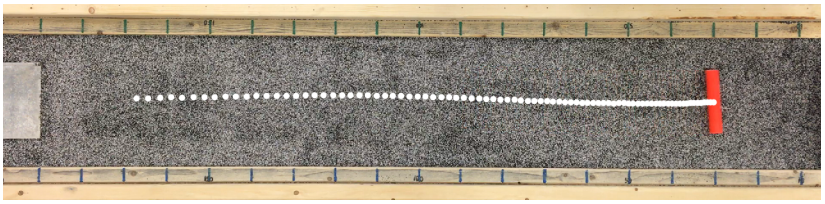

Figure 2: Final frame of a trial with the corresponding image trajectory plotted in white.

(iii) Object trajectories

The camera and scene calibrations were used to convert the image trajectories into object trajectories of the (X, Y) position of the cylinder centers over time for each trial. In a given scene, each image coordinate is the projection of an entire ray in the object coordinate space. If one of the object coordinates of a point is known, however, the degeneracy can be broken and the projection inverted to determine the two remaining unknown object coordinates from the image coordinates. For each trial, we used the vertical offset of the material surface from the side rails and the radius of the cylinder to estimate the height Z of the plane containing the cylinder center. Assuming that the ray corresponding to the cylinder's image position passes through the center of the cylinder, the inversion of the image position at this Z yields an estimate of the (X, Y) coordinates of the center of the cylinder. Typical gradients in our projection inversion are approximately $1\,\mathrm{mm}$ of X or Y displacement per image pixel. The characteristic $\sim 3\,\mathrm{px}$ reprojection error in the camera calibration therefore corresponds to a $\sim 3\,\mathrm{mm}$ systematic uncertainty in the absolute positions in our object trajectories.

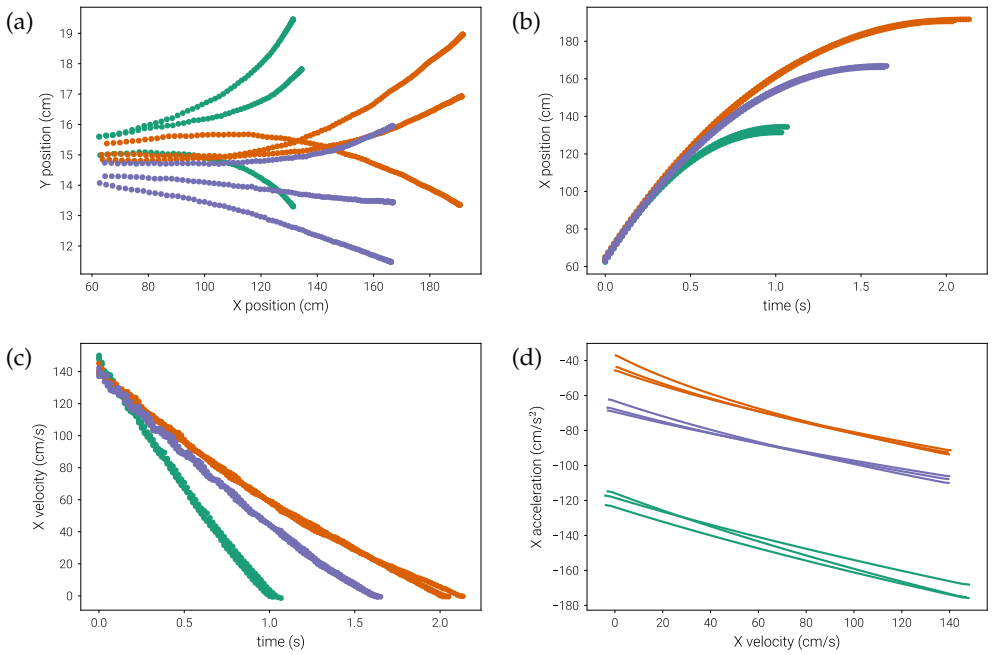

Figure 3: All trajectories for cylinder 24 (green), 29 (blue), and 36 (orange) on ballotini. (a) Two-dimensional trajectories across the bed. (b) Along-channel positions over time. (c) Along-channel velocities over time. (d) Along-channel accelerations versus velocity, from least-squares quadratic fits to the velocity data.

(c) Results

We initially tilted the channel by supported it at different heights under the two ends, and varied the angle to look for steady rolling states. We found, however, that the channel was insufficiently stiff and would flex under its own weight, resulting in further errors in the calibration procedure, as well as a spatially-varying downslope component of gravity. To avoid these issues, we laid the channel on the flat with distributed supports to keep it straight to within our $\sim 1\,\mathrm{mm}$ measurement precision. Removing any gravitational acceleration along the bed had the further advantage of ensuring that the rolling resistance was more easily measured.

In our preliminary experiments on the sand, we also explored the effect of the length of the cylinders and the depth of the granular bed. With cylinders of the same PVC piping but different lengths, we found that there were no significant differences in the trajectories. Similarly, for trials using 1, 3, 5, 7, and $9\,\mathrm{cm}$ deep beds, we again found no significant or systematic effect on the trajectories. We therefore decided to fix the cylinder lengths to be $15\,\mathrm{cm}$ and the depth of the bed to be $7\,\mathrm{cm}$ for the sand and $2\,\mathrm{cm}$ for ballotini to reduce the number of parameters being varied. With these considerations, we built a dataset for over 450 trials. Plots of the trajectories for several cylinders on the ballotini are shown in Figure 3.

Two dimensional $X - Y$ plots of the trajectory are useful for identifying trials in which a cylinder swerved to the side and rolled close to the side-rails, where it visibly tended to slow down. Some trials also abruptly changed direction on approaching the side-rails, at times turning further towards the side, and at other times veering back towards the center of the channel. Since most trajectories remained close to the center of the bed, we used the X components of the trajectories to study the one-dimensional kinematics of the cylinders, and eliminated the trials in which the cylinder veered too far off centre (see §4).

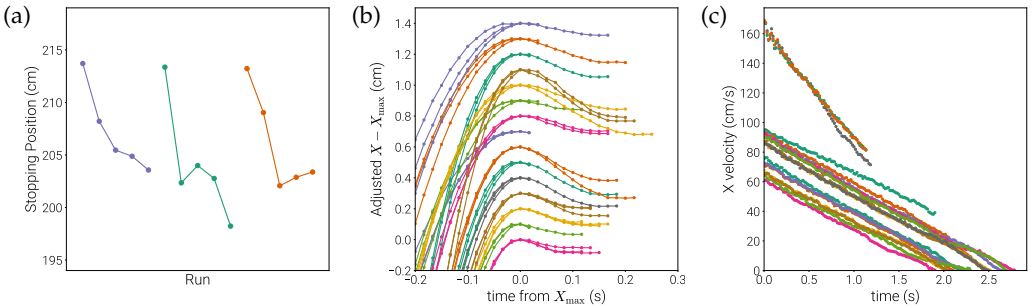

Figure 4: (a) Stopping distances of cylinders 23, 24 and 25 on sand in successive trials. (b) Rollback of cylinders on ballotini, with positions and times relative to maximum X position and adjusted to separate by cylinder. (c) Along-channel velocities over time of cylinder 23 on sand.

The millimeter-scale accuracy of the position determination allowed us to use finite differences in time to generate downslope velocities. Further differentiation to determine the acceleration, however, was precluded by the noise in the position measurements. In figure 3, the cylinder accelerations are instead estimated by differentiating linear least squares fits of quadratic polynomials to the velocity data in panel (c). In general, however, we found that the form of such fits often severely biased the shape of the resulting acceleration-velocity curves (panel (d)), and ultimately, we favoured the forward-modelling approach of § 4 for determining the dependence of acceleration on velocity.

For trials on the sand, where the surface was not reset between each run, we observed a systematic change in the stopping distances of the cylinders when they were first rolled over a fresh surface. We attributed this to a superficial compaction and smoothing of the top layers of grains, which affected the rolling resistance. To eliminate this affect and begin with a runway that accommodated any sideways migration of our 15cm-long cylinders, we therefore followed a bedding-in procedure at the beginning of the experiments: we first rolled a much longer (25cm) cylinder down the track repeatedly until the stopping distance varied much less. Despite this preliminary preparation of the surface, there were still noticeable changes in the rolling resistance when cylinders were switched, with the stopping distances of the first few trials systematically increasing or decreasing until saturating, typically $\sim 10\,\mathrm{cm}$ away from the first roll with that cylinder (Figure 4(a)). After 3 or more trials, the stopping distance was typically reproducible to within $\sim 2\,\mathrm{cm}$ centimeters. Evidently, each cylinder affects the surface of the track slightly differently, but we did not explore this effect in any further detail.

Another interesting feature of the rolling dynamics arose at the end of the trajectories where the cylinders came to a stop on the bed. As shown in Figure 4(b), the cylinders tend to roll backwards several millimeters before coming to a complete stop. This effect may be due to the mound of grains, or "bow wave", that builds up ahead of the cylinder, and which transmits the forces from the bed during rolling. Once the cylinder is arrested, however, the horizontal bed reaction becomes unbalanced, momentarily pushing the cylinder backwards.

We conducted trials with a range of initial velocities for each cylinder on the sand. For initial velocities in the range of $50 - 100\,\mathrm{cm/s}$, the deceleration of the cylinders did not show a pronounced dependence on the initial velocity, as can be seen in Figure 4(c). Trials with higher initial velocities around $175\,\mathrm{cm/s}$, however, showed substantially larger decelerations. It was difficult to produce consistent trials at these speeds, as the cylinders would frequently bounce after leaving the ramp and veer abruptly into the side rails. We therefore excluded these higher-velocity runs from the bulk of our analysis, but the discrepancies in Figure 4(c) suggest that efforts to characterize resistance in terms of only rolling speed may well conceal the full nature of the dynamics.

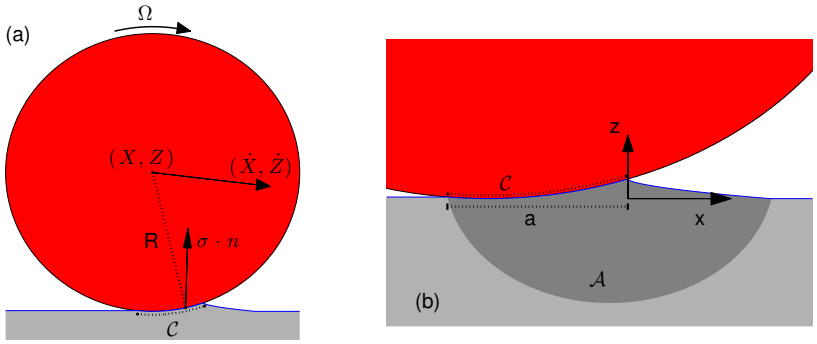

Figure 5: (a) Geometry of a rigid cylinder rolling on a deformable surface. (b) Magnification of the flowing region (dark gray, labelled $\mathcal{A}$) under the cylinder.

Taking $50\,\mathrm{cm/s}$ as a characteristic velocity, $6\,\mathrm{cm}$ as a characteristic cylinder diameter, and $\nu \approx 1.5 \times 10^{-5}\,\mathrm{m^2/s}$ for the kinematic viscosity of air, we estimate the Reynolds number of the airflow around the cylinders as they roll down the bed to be of order $\mathrm{Re} \sim 2000$. We therefore expect the air drag on the cylinders to depend quadratically on velocity with an order-one drag coefficient. To directly measure the effect of air resistance, we performed additional trials in which we rolled the cylinders over a glass sheet placed on the channel (reported in § 4).

3. Modeling

(a) Cylinder dynamics

To model the dynamics, we consider the motion of a two-dimensional rigid cylinder rolling over a deformable granular surface. The geometry is sketched in Figure 5. We use a new cartesian coordinate system centered under the leading contact point at the neutral surface of the sand, with x pointing forward and z upward. The cylinder has radius R, mass per unit length M, and moment of inertia per unit length I. The cylinder has velocity $(\dot{X}(t), \dot{Z}(t))$ and clockwise rotation rate $\Omega(t)$. The translational and rotational dynamics of the cylinder are given by:

$$M\ddot{X} = F_x \tag{3.1}$$

$$M\ddot{Z} = F_z - Mg \tag{3.2}$$

$$I\dot{\Omega} = -T \tag{3.3}$$

where g is gravity, and (F_x, F_y) and T are the contact force and anti-clockwise torque from the underlying medium, again per unit length of the cylinder.

We write $I = \alpha M R^2$, where α is a dimensionless description of the radial mass distribution of the cylinder, with $\alpha = 1/2$ for a uniform solid cylinder, and $\alpha \to 1$ for a thin cylindrical shell. The contact forces are computed by integrating the surface stresses over the contact arc $\mathcal{C}$ as

$$\begin{pmatrix} F_x \\ F_z \end{pmatrix} = \int_{\mathcal{C}} \boldsymbol{\sigma} \cdot \mathbf{n}\, \mathrm{d}\ell, \tag{3.4}$$

where $\boldsymbol{\sigma}$ is the granular stress tensor, and $\mathbf{n}$ and ℓ denote the normal and arc length along $\mathcal{C}$. The torque around the cylinder center is given by

$$T = \int_{\mathcal{C}} (-R\hat{\mathbf{e}}_z + \mathbf{r}) \times \boldsymbol{\sigma} \cdot \mathbf{n}\, \mathrm{d}\ell = RF_x + \int_{\mathcal{C}} \mathbf{r} \times \boldsymbol{\sigma} \cdot \mathbf{n}\, \mathrm{d}\ell, \tag{3.5}$$

where $\mathbf{r}$ is the position vector from the bottom of the cylinder.

The horizontal and angular momentum equations can be combined to give

$$M(\ddot{X} + \alpha R\dot{\Omega}) = F_x - \frac{T}{R} = -\frac{1}{R}\int_{\mathcal{C}} \mathbf{r}\times\boldsymbol{\sigma}\cdot\mathbf{n}\,\mathrm{d}\ell. \tag{3.6}$$

If rolling occurs without without slip, $R\Omega = \dot{X}$, and the left side of (3.6) becomes $(1+\alpha)M\ddot{X}$. Indeed, the experimental cylinders exhibit no obvious sliding over the granular surface: $\dot{X}$ was unmeasurably different from $R\Omega$ to within our experimental precision (based on tracking surface markers on the cylinder surfaces). Thus, the horizontal dynamics are directly controlled by the rolling resistance,

$$F_r = \frac{1}{R}\int_{\mathcal{C}} \mathbf{r}\times\boldsymbol{\sigma}\cdot\mathbf{n}\,\mathrm{d}\ell. \tag{3.7}$$

Below, we evaluate the integrals in (3.4) and (3.7) to leading order in the small parameter a/R, where a is the horizontal length of the contact arc, treating the sand as a plastic material satisfying the Mohr-Coulomb constitutive law. Before accomplishing this feat, we note that if the surface stresses are $O(\rho_s g a)$, then F_x and F_z are $O(\rho_s g a^2)$, while F_r is $O(\rho_s g a^3/R)$. But F_x and F_r must be of similar order according to (3.1) and (3.6), which can only be arranged if F_x turns out to contain a small numerical factor of order a/R. This observation, which plays a key role below, implies that $\ddot{X} = O(aF_z/RM)$. Moreover, in order that the contact area remain small during rolling, the vertical velocity and acceleration must be $O(a/R)$ in comparison to $\dot{X}$ and $\ddot{X}$. Thus, $M\ddot{Z} = O(a^2F_z/R^2)$, and so, to leading order, the roller is vertical equilibrium, $F_z \approx Mg$. Hence, $\ddot{X} = O(ag/R) \ll g$, in line with the measured cylinder decelerations (see figure 3), and $(a/R) \sim R^{-1}\sqrt{M/\rho_s} \sim \sqrt{\rho_c/\rho_s}$, which is about 0.5 for the experimental cylinders. More refined computations of the granular force lead to smaller estimates of a/R as we indicate later.

(b) Sand dynamics

(i) Slipline theory

Ignoring inertia, the equations of force balance for the granular stresses are

$$\frac{\partial\sigma_{xx}}{\partial x} + \frac{\partial\sigma_{xz}}{\partial z} = 0 \qquad \& \qquad \frac{\partial\sigma_{xz}}{\partial x} + \frac{\partial\sigma_{zz}}{\partial z} = \rho_s g, \tag{3.8}$$

where ρ_s is the sand density and g is gravitational acceleration. For the stresses, we use the Mohr-Coulomb plastic constitutive law [23], which we write in the form,

$$\begin{aligned} \sigma_{xx} &= -p + p\sin\phi\cos 2\theta \\ \sigma_{zz} &= -p - p\sin\phi\cos 2\theta \\ \sigma_{xz} &= p\sin\phi\sin 2\theta, \end{aligned} \tag{3.9}$$

where ϕ is the internal angle of friction, p is the mean compressive stress, and θ represents the angle between the direction of the least compressive stress and the horizontal. With this rheology the stress field is conveniently represented in terms of its characteristic curves, the sliplines. These curves are composed of two families; the $\alpha-$lines are defined by

$$\mathrm{d}z = \tan(\theta - \varepsilon)\,\mathrm{d}x, \quad \mathrm{d}p + 2p\tan\phi\,\mathrm{d}\theta = -\rho_s g(\mathrm{d}z + \tan\phi\,\mathrm{d}x), \tag{3.10}$$

whereas the $\beta-$lines satisfy

$$\mathrm{d}z = \tan(\theta + \varepsilon)\,\mathrm{d}x, \quad \mathrm{d}p - 2p\tan\phi\,\mathrm{d}\theta = -\rho_s g(\mathrm{d}z - \tan\phi\,\mathrm{d}x), \tag{3.11}$$

with

$$\varepsilon = \frac{\pi}{4} + \frac{\phi}{2}. \tag{3.12}$$

(ii) Boundary conditions

We calculate the leading-order forces in the small parameter a/R, for which it is sufficient to linearise the surface conditions about $z = 0$. In the coordinate system centered at the leading edge, the section $-a < x < 0$ is the contact surface $\mathcal{C}$, and the section $x > 0$ is a free surface.

We impose a friction condition beneath the cylinder that translates to demanding that

$$\theta = \theta_f \quad \text{on} \;\; z = 0, \;\; -a < x < 0. \tag{3.13}$$

If the surface is perfectly smooth, $\theta_f = 0$ (so that $\sigma_{xz} = 0$ and $\sigma_{zz} = -p(1 + \sin\phi)$). If it is perfectly rough, $\theta_f = -\varepsilon$ (so that the $\beta-$lines are parallel to the surface). If δ denotes the surface friction angle, then $\theta_f = \frac{1}{2}\delta + \frac{1}{2}\sin^{-1}(\sin\delta/\sin\phi)$.

The free surface ahead of the footing is in a state of compression with

$$p = 0, \quad \theta = \tfrac{1}{2}\pi, \quad \text{on} \;\; z = 0, \;\; x > 0 \tag{3.14}$$

(so that $\sigma_{xz} = \sigma_{zz} = 0$). This leads to a subsurface triangular region (a "Rankine zone") where the stress is hydrostatic ($\sigma_{zz} = \rho_s g z$ and $p = -\rho_s g z/(1 - \sin\phi)$), and the characteristics are straight and inclined at angles $\pm\varepsilon$ to the vertical.

(iii) Separable solution

The problem permits a self-similar solution corresponding to a separable form in polar coordinates (r, ψ) [23]. We set

$$x = r\cos\psi \equiv \Xi\xi(\psi), \quad z = r\sin\psi \equiv \Xi\zeta(\psi), \quad p = \rho_s g r \Sigma(\psi), \quad \theta = \Theta(\psi), \tag{3.15}$$

where Ξ is an undetermined lengthscale. The stress equations then reduce to

$$\Sigma' = \frac{\Sigma\sin(2\Theta - 2\psi) - \cos(2\Theta - \psi)}{\sin\phi + \cos(2\Theta - 2\psi)} \tag{3.16}$$

$$\Theta' = \frac{\sin\psi + \sin\phi\sin(2\Theta - \psi) + \Sigma\cos^2\phi}{2\Sigma\sin\phi[\sin\phi + \cos(2\Theta - 2\psi)]}. \tag{3.17}$$

Note that there are singular points in the system (3.16)-(3.17) at $\sin\phi + \cos(2\Theta - 2\psi) = 0$. One such point always occurs at the border with the triangular Rankine zone ahead of the self-similar region where we must impose the boundary condition

$$\Theta(\varepsilon - \tfrac{1}{2}\pi) = \tfrac{1}{2}\pi, \tag{3.18}$$

to match to the Rankine zone. Here, we further demand that the solution be regular, which automatically sets the pressure to its hydrostatic value, implying $\Sigma(\varepsilon - \frac{1}{2}\pi) = -\sin\psi/(1 - \sin\phi)$, without explicitly adding this as a second boundary condition.

For $\psi \to -\pi$, we impose $\Theta(-\pi) = \theta_f$. For the perfectly rough case when $\theta_f = -\varepsilon$, this second boundary is also a singular point. Moreover, we cannot impose regularity in view of the imposition of all the boundary conditions already. Instead, the derivative of the solution diverges and we exploit the local solution,

$$\Theta + \varepsilon \sim \sqrt{\frac{|\psi + \pi|\,[1 + \Sigma(-\pi)\cot\phi]}{2\Sigma(-\pi)}}, \tag{3.19}$$

to impose the boundary condition at an angle slightly below $-\pi$. Numerical solutions for rough, semi-rough and smooth cylinders are shown in figure 6.

Given $\xi(\psi) = \zeta(\psi)\cot\psi$ along each characteristic, we have

$$\zeta' = \frac{\zeta\sec^2\psi\cot\psi}{1 - \tan\psi\cot(\Theta \mp \varepsilon)}. \tag{3.20}$$

We may solve this ODE subject to $\zeta \to 0$ for $\psi \to -\pi$, implying $\xi \to -1$. The resulting curves $(x, y) = \Xi(\xi_{\alpha,\beta}(\psi), \zeta_{\alpha,\beta}(\psi))$, corresponding to the two choices of sign in (3.20), generate the slipline field through the scaling Ξ. Examples are shown in figure 7.

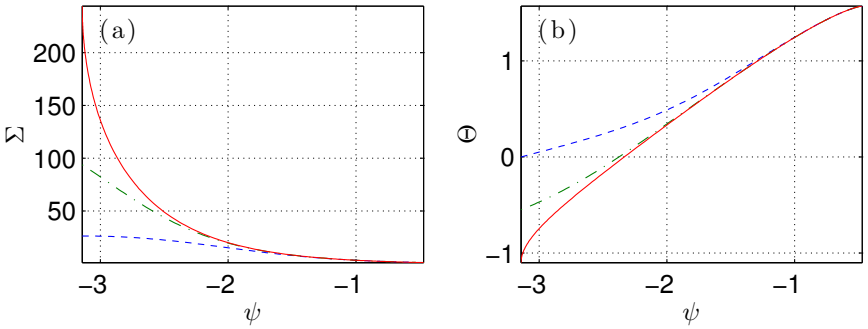

Figure 6: Self-similar solution for (a) $\Sigma(\psi)$ and (b) $\Theta(\psi)$ for rough ($\theta_f = -\varepsilon$; solid), smooth ($\theta_f = 0$; dashed) cylinders and semi-rough ($\theta_f = -\frac{1}{2}\varepsilon$; dot-dashed), with $\phi = 36^\circ$.

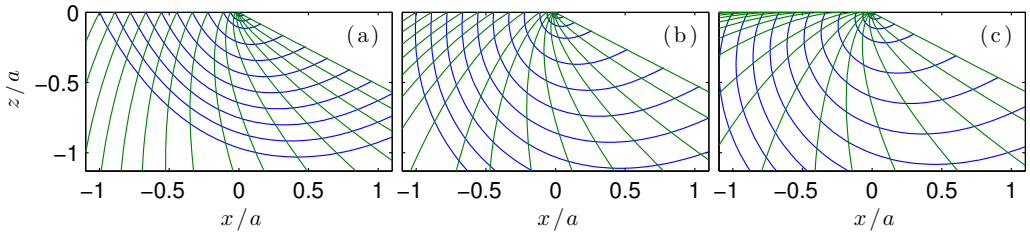

Figure 7: Self-similar slipline fields with $\phi = 36^\circ$ for cylinders with (a) smooth ($\theta_f = 0$), (b) semi-rough ($\theta_f = -\frac{1}{2}\varepsilon$), and (c) rough ($\theta_f = -\varepsilon$) surfaces.

(iv) Collins construct

As seen below, the surface forces acting on the cylinder that are predicted by the separable solution cannot be adjusted to ensure that $F_x = O(\rho_s g a^3/R)$ in accordance with the cylinder dynamics discussed in § 3(a). This motivates a modification of the separable solution that follows Collins' solution for a cohesive ideal plastic deforming underneath a roller [25]. More specifically, we rigidly attach a plug of grains to the surface of the cylinder, such that the roller and plug rigidly rotate about a point (x_o, z_o) beneath the granular surface. The rotation centre must lie along the line connecting the back contact point with the centre of the cylinder. If we define Υ to be the angle that line makes with the vertical, and $a\ell$ to be the distance from (x_o, z_o) to the back contact point, then

$$(\dot{X}, \dot{Z}) = (R + a\ell)\Omega(\cos\Upsilon, -\sin\Upsilon). \tag{3.21}$$

But $a \ll R$ and $\dot{Z} = O(a\dot{X}/R)$, demanding that $\Upsilon = O(a/R)$, $(x_o, z_o) \sim -a(1, \ell)$, and

$$\dot{X} = R\Omega + a\ell\Omega + O(a^2\Omega/R), \tag{3.22}$$

as illustrated in figure 8. Thus, there is an effective slip, with speed $\dot{X} - R\Omega \approx a\ell\Omega$, even though there is no true slip between the surfaces.

Ahead of the plug, the material deforms plastically and the separable solution applies. Because the border between the rotating plug and this plastic region is a yield surface, it must also follow a slip-line; we choose this to be a specific one of the self-similar β-lines intersecting the contact surface at $(-x_\beta, 0)$ (see figure 8). This $\beta-$line continues down to the point P where it intersects the lowest $\alpha-$line, which bounds the entire yielded region. The left-hand border of the rotating plug, on the other hand, divides that region from the immobile grains below, and must therefore be a circular failure surface. This arc continues the lowest $\alpha-$line to the origin, and meets that

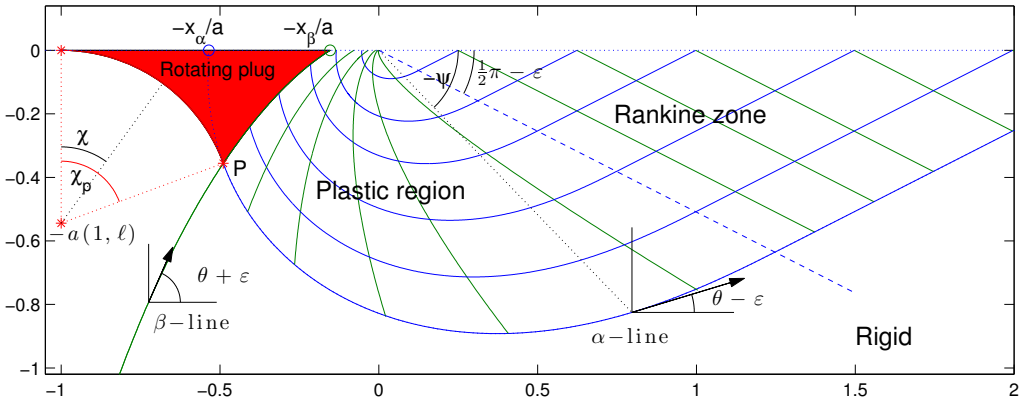

Figure 8: Sketch of the geometry for the Collins slipline solution in the limit of small deformation. The angle subtended by the rotating plug is $\chi_p \equiv \varepsilon - \Theta(\psi_p)$. The slipline field is plotted for $\phi = 36^\circ$, $\theta_f = -\frac{1}{2}\varepsilon$ and $\psi_p = -4\pi/5$.

characteristic tangentially at the point P. This geometry demands that

$$\ell = \frac{-\sin\psi_p}{\cos[\psi_p + \varepsilon - \Theta(\psi_p)] - \cos\psi_p}, \tag{3.23}$$

where ψ_p is the polar angle of the intersection point. The lowest $\alpha-$line is given by $x_\alpha(\xi_\alpha, \zeta_\alpha)$, and the $\beta-$line bordering the rotating plug is $x_\beta(\xi_\beta, \zeta_\beta)$, where

$$x_{\alpha,\beta} = -\frac{a\ell\{1 - \cos[\varepsilon - \Theta(\psi_p)]\}}{\zeta_{\alpha,\beta}(\psi_p)}. \tag{3.24}$$

The stress along the circular failure surface underlying the rotating plug is not given by the separable solution. Instead, the requirement that this arc continues the lowest $\alpha-$line, in conjunction with its circular shape implies that

$$\frac{\mathrm{d}p}{\mathrm{d}\chi} = 2p\tan\phi - \rho_s g a\ell(\sin\chi - \tan\phi\cos\chi). \tag{3.25}$$

where χ is the angular position along the arc measured from the vertical, and $\theta = \varepsilon - \chi$. Equation (3.25) can be integrated using the boundary condition that the pressure matches with that of the separable solution at the bottom point of the plug ($\chi = \chi_p$ in figure 8).

(v) Forces and torques

Let $\mathcal{L}$ denote the contour combining the circular arc and $\beta-$line that border the plug with the section of the contact surface from $(-x_\beta, 0)$ to the origin. The forces acting on this contour are the same as the forces acting on the cylinder modulo the contributions from the weight of the rotating plug. We therefore write the forces in (3.4) and (3.7) as

$$F_x = \hat{F}_x, \qquad F_z = \hat{F}_z - \int\!\!\int_A \rho_s g \,\mathrm{d}A, \qquad F_r = \hat{F}_r - \int\!\!\int_A (a + x)\rho_s g \,\mathrm{d}A, \tag{3.26}$$

where the integrals are taken over the area A of the plug, and where $\hat{F}_x$, $\hat{F}_z$ and $\hat{F}_r$ are the forces acting on $\mathcal{L}$. These are given by

$$\begin{pmatrix} \hat{F}_x \\ \hat{F}_z \end{pmatrix} = \int_{\mathcal{L}} p \begin{pmatrix} 1 - \sin\phi\cos 2\theta & -\sin\phi\sin 2\theta \\ -\sin\phi\sin 2\theta & 1 + \sin\phi\cos 2\theta \end{pmatrix} \cdot \boldsymbol{n}\,\mathrm{d}s, \tag{3.27}$$

and

$$\hat{F}_r = \frac{1}{R}\int_{\mathcal{L}} \mathbf{r}\times p \begin{pmatrix} 1 - \sin\phi\cos 2\theta & -\sin\phi\sin 2\theta \\ -\sin\phi\sin 2\theta & 1 + \sin\phi\cos 2\theta \end{pmatrix} \cdot \boldsymbol{n}\,\mathrm{d}s \tag{3.28}$$

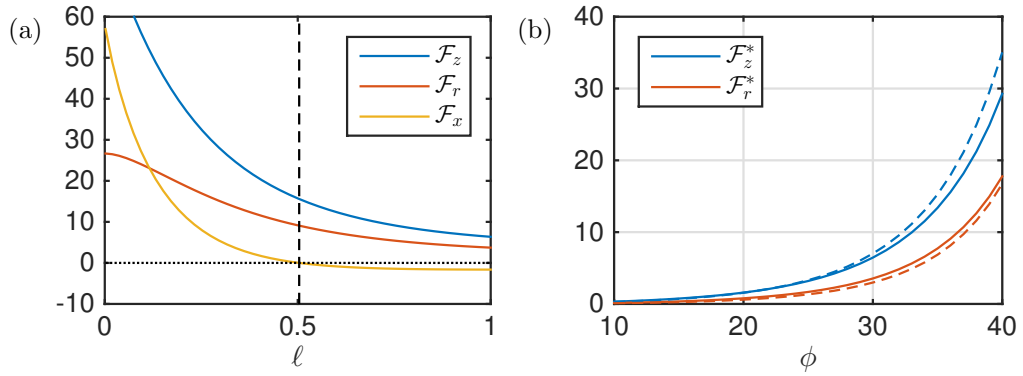

Figure 9: (a) Dimensionless force functions for the Collins solution, for $\phi = 36^\circ$ and a perfectly rough cylinder. The vertical dashed line indicates the location $\ell = \ell_*$ at which $\mathcal{F}_x = 0$. (b) Lift force $\mathcal{F}_z^* = \mathcal{F}_z(\ell_*; \phi, \theta_f)$ and rolling resistance $\mathcal{F}_r^* = \mathcal{F}_r(\ell_*; \phi, \theta_f)$ as a function of internal frictional angle. Solid lines show the perfectly rough case; dashed lines show the result for $\theta_f = -\varepsilon/10$.

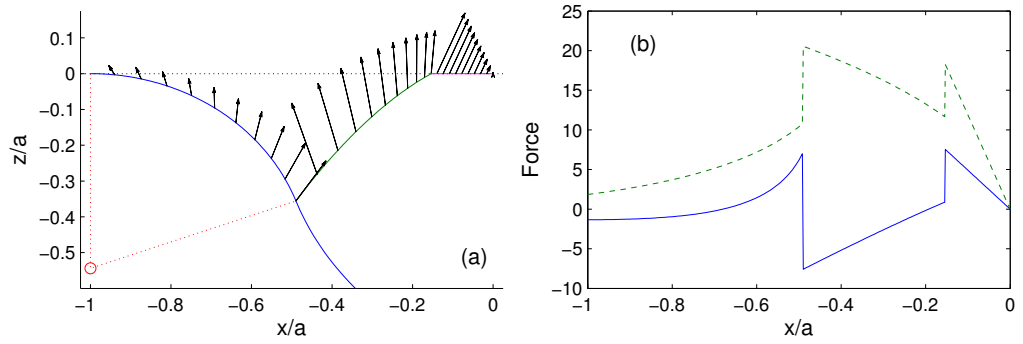

Figure 10: Breakdown of the contributions to the dimensionless horizontal and vertical force on the contour $\mathcal{L}$ for the solution shown in figure 8; (a) shows force vectors (per unit length), whereas (b) plots the horizontal (solid) and vertical (dashed) components.

where $\mathbf{n}$ denotes the outward normal to $\mathcal{L}$. These integrals can be calculated using the separable solution and (3.25) for p and θ. Since the pressure scales with the weight of the material, $\rho_s g a$, the contact length a can be scaled out and the resulting forces written in terms of dimensionless functions as

$$F_x = \rho_s g a^2 \mathcal{F}_x(\ell; \phi, \theta_f) \qquad F_z = \rho_s g a^2 \mathcal{F}_z(\ell; \phi, \theta_f) \qquad F_r = \frac{a}{R} \rho_s g a^2 \mathcal{F}_r(\ell; \phi, \theta_f). \tag{3.29}$$

Sample solutions for the force functions $\mathcal{F}_x(\ell; \phi, \theta_f)$, $\mathcal{F}_z(\ell; \phi, \theta_f)$ and $\mathcal{F}_r(\ell; \phi, \theta_f)$ are shown in figure 9(a) for a perfectly rough cylinder with $\phi = 36^\circ$. The contributions to the horizontal and vertical forces, $\mathcal{F}_x$ and $\mathcal{F}_z$, for a specific choice of ℓ (corresponding to the solution in figure 8) are shown in figure 10. The forces distributions for the separable solution grow linearly with position along the line of contact as indicated by the plots for $x > -x_\beta$ in (b); the redistribution of stress along the contour $\mathcal{L}$ due to the presence of the rotating plug modifies the total bed reaction, reducing $\mathcal{F}_x(\ell)$ and generating stress jumps at the switches between the different pieces of $\mathcal{L}$.

As argued earlier, the angular and horizontal accelerations can only be consistent with one another provided that F_x is small. In particular, we must have $\mathcal{F}_x = O(a/R)$, which demands that ℓ must be close to the value $\ell = \ell_*$ that gives $\mathcal{F}_x(\ell_*; \phi, \theta_f) = 0$. Note that the result for the

separable solution (with no attached plug) is recovered by taking $\ell = 0$, which indicates that this case cannot furnish consistent horizontal and angular accelerations on the cylinder.

To leading order we therefore find

$$F_z \sim \rho_s g a^2 \mathcal{F}_z^* \qquad \text{and} \qquad F_r \sim \frac{a}{R} \rho_s g a^2 \mathcal{F}_r^*, \tag{3.30}$$

where $[\mathcal{F}_z^*, \mathcal{F}_r^*] \equiv [\mathcal{F}_z(\ell_*; \phi, \theta_f), \mathcal{F}_r(\ell_*; \phi, \theta_f)]$. The two special values $\mathcal{F}_z^*$ and $\mathcal{F}_r^*$ are plotted as functions of ϕ in figure 9(b) for a perfectly rough cylinder and one with a semi-rough surface. Even though the semi-rough case is almost smooth ($\theta_f = -\varepsilon/10$), the change in the dimensionless force function is very slight. Thus, the rolling resistance is expected to be insensitive to the roughness of the surface of the cylinder. One could also envision a situation in which the cylinder slides over the granular bed (and the rotating plug) in the manner of true slip when the net normal force over the contact line is too small in comparison to the total tangential force. This situation is ruled out (for surface friction coefficients of order unity) when $\ell \sim \ell_*$, as this guarantees that the tangential force on the surface is $O(a/R)$ relative to the normal force.

In Appendix A, we proceed further with the model and also compute the velocity field of the deforming granular bed, which allows one to determine the shape of the free surface in the bow wave ahead of the roller. Two significant problems emerge with this construction on using traditional Mohr-Coulomb model: the leading-order velocity field diverges at the front contact point and the free surface descends unphysically below the bottom of the rolling cyinder. Both problems are absent for a cohesive material (Appendix B), and arise here because the standard Mohr-Coulomb model predicts an excessive degree of dilation during flow, which is a known deficiency of that theory [29,30] and can be cured by introducing a relatively small angle of dilation (see Appendix A).

4. Analysis

To compare with the predictions of the plasticity theory, we fit the experimental data to model trajectories given by a force law with constant and quadratic velocity terms:

$$\ddot{X} = C_0 + C_2 \dot{X}^2. \tag{4.1}$$

Before performing the fit, we first removed any trials on the sand that either strayed more than $4\,\mathrm{cm}$ from the center of the track, or showed an obvious re-bedding behaviour (typically the first two runs after switching cylinders). We next truncated the remaining trajectories once their velocity dropped below approximately $5\,\mathrm{cm/s}$ to prevent the roll-back effect of figure 4(b) (which cannot be captured by the model in (4.1)) from affecting the parameters of the fit. We then performed a nonlinear least-squares fit to the solution of (4.1) of the data for all trials with a given cylinder and granular material, using the initial position and velocity for each trial, and the force-law coefficients C_0 and C_2 as parameters. Uncertainties in the fited parameters were determined using the covariances from the nonlinear fit, scaled by the square-root of the 95th percentile of the corresponding χ^2 distribution, with the uncertainties in the position data all taken to be $3\,\mathrm{mm}$.

Figure 11 shows the fitting results for trials on the glass sheet, sand, and ballotini. The fits for the glass sheet imply a small constant resistance and a more substantial quadratic component, suggesting that air drag provides the dominant resistance in these trials. In that situation, C_0 would be negligible and C_2 would be related to the cylinder's drag coefficient C_d by

$$C_2 = -\frac{1}{2\pi} \frac{\rho_a}{\rho_c} \frac{C_d}{R(1+\alpha)}. \tag{4.2}$$

The average of the C_2 fits suggests that $C_d = 2.7 \pm 0.3$ for cylinders rolling on a flat surface.

For most cylinders on both the ballotini and sand, the fitted values of C_0 and C_2 indicate that the velocity-dependent component of the acceleration is less significant than the constant drag at the typical velocities of our trials. The ballotini shows a substantially larger constant resistance than the sand, but the two typically show comparable quadratic coefficients. In both cases, the

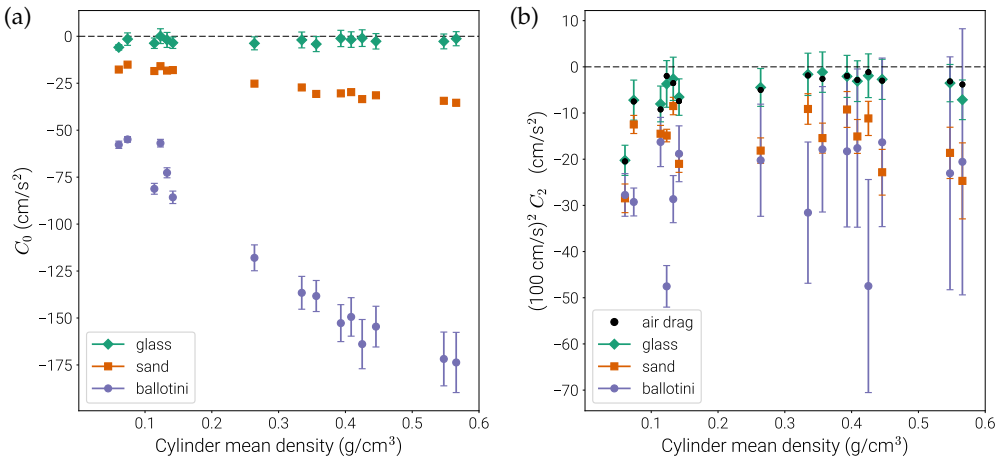

Figure 11: Best fitting force-law coefficients for cylinders rolling on the glass sheet, aquarium sand, and ballotini, showing (a) C_0 and (b) C_2 in (4.1). In (b), the points labelled "air drag" refer to the estimate (4.2) with $C_d = 2.7$.

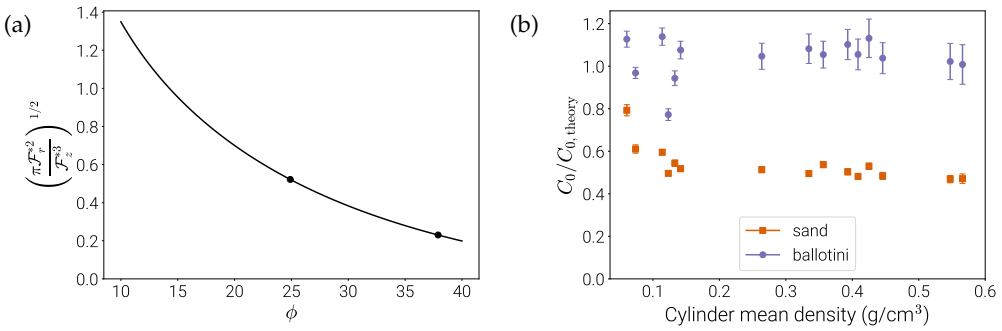

Figure 12: (a) Predicted factor in rolling resistance (4.4) as a function of internal friction angle. (b) Comparison between the fitted resistance values and the expected resistance from the model, assuming the cylinders to be in vertical equilibrium.

fitted C_2 values are roughly an order of magnitude larger than that expected from air resistance, indicating that there is a velocity-dependent rolling resistance for these materials.

If we again assume that the cylinder is in vertical equilibrium ($F_z = Mg$), the leading-order vertical force prediction from the model can be used to solve for the contact length a as

$$\left(\frac{a}{R}\right)^2 = \frac{\rho_c}{\rho_s}\frac{\pi}{\mathcal{F}_z^*}. \tag{4.3}$$

This estimate improves the prediction from dimensional analysis given earlier and suggests that $a/R \approx 0.1 - 0.2$ or $0.2 - 0.6$ for our experiments with sand and ballotini, respectively. The leading-order prediction for the rolling resistance prediction can now be written as the constant acceleration,

$$C_{0,\text{theory}} = -\frac{g}{1+\alpha}\left(\frac{a}{R}\right)\frac{\mathcal{F}_r^*}{\mathcal{F}_z^*} = -\frac{g}{1+\alpha}\left(\frac{\rho_c}{\rho_s}\right)^{1/2}\left(\frac{\pi\mathcal{F}_r^{*2}}{\mathcal{F}_z^{*3}}\right)^{1/2}. \tag{4.4}$$

The final factor in (4.4) is plotted as a function of internal friction angle in figure 12(a). Somewhat counter to intuition, this factor decreases with the internal friction because, although the drag force F_r increases with ϕ, the contact area needed to support the weight of the cylinder decreases more strongly with friction. In other words, the roller digs into the medium less for higher ϕ to reduce the rolling resistance, as seen in the experiments where the cylinders encounter greater resistance when rolling over the ballotini in comparison to sand. A more detailed comparison of theory and experiment is shown in figure 12(b), which shows the ratio between the model prediction in (4.4) and the fitted C_0 values for sand and ballotini. The theory over-predicts the fitted resistance on the sand by roughly a factor of 2, but matches that for the ballotini to within about 20%. The model therefore correctly captures the overall magnitude of the rolling resistance and its scaling with the cylinder's mean density.

Unfortunately, the trajectory fits typically show strong covariances between C_2 and the initial velocities of the faster trials, which limits our confidence in the inferred values of these parameters. Moreover, different forms for the velocity dependence of the force law (such as a linear form) lead to trajectories that do not fit the data any more or less conclusively. We cannot therefore characterize the velocity dependence of the resistance in any further detail.

5. Conclusion

In this paper we have experimentally investigated the resistance experienced by cylinders rolling on two dry granular media, a relatively coarse sand and ballotini (glass spheres). The cylinders were relatively long and light, with low mean densities compared to the granular material (which distinguishes our study from some earlier experiments with spheres [16] and the bulk of the literature on wheels). Thus, surface deformations are expected to be localized and superficial. This leads us to model the bed as two-dimensional and in the asymptotic limit that the deforming contact region is much smaller than the cylinder radius and the deflection of the free surface is slight [18–20]. We further adopted the cohesionless Mohr-Coulomb law to describe the granular rheology. The model predicts that the rolling resistance is independent of cylinder velocity, scaling with the square-root of the ratio of mean densities.

The trajectories of cylinders in the experiment were fitted using a simple drag law in which rolling resistance consisted of an overall constant plus a rate-dependent part that was quadratic in cylinder speed, similar to that expected for air drag. The measured drag was dominated by the constant term at the velocities typical of our experiments. However, the quadratic component was not negligible and larger than that expected for air drag, which was estimated by rolling the cylinders down a flat glass surface. Thus, the rolling resistance appears to contain an effect stemming from rate-dependent granular rheology. We did not, however, attempt to include such effects into the rheology of our theoretical model, as might be feasible by exploiting recently proposed semi-empirical friction laws [17].

Nevertheless, the basic drag constant measured in the experiments is, to within a factor of two, consistent with that predicted by the Mohr-Coulomb plasticity model, reproducing the dependence on the ratio of mean densities. One important feature of the model is the characteristic flow pattern assumed underneath the rolling cylinder. Following Collins [25], we have represented this pattern in terms of a region of plastic deformation below the front contact point which extends up to the free surface ahead of the cylinder, and back to a plug behind that is rigidly attached to the roller. The plug rigidly rotates with the cylinder and slides along a circular failure surface over the static grains underneath. The rotating plug incorporates a finite, but small, effective slip of the cylinder as it rolls due to granular deformation, as in Reynolds' [5] original image of the mechanism underlying rolling friction. Crucially, the plug also re-orientates the forces that are exerted on the cylinder by the bed such that the net horizontal force can be made small in accordance with the equations of motion of the cylinder. Without this re-orientation, there is a physical inconsistency between the angular and horizontal momentum equations that precludes a rolling state.

Several extensions to the experiments may allow a better determination of rolling resistance on granular media: a longer bed would permit one to record trajectories with a larger range of velocities, and further improvement of the scene calibration would allow better inference of cylinder trajectories in physical space, both of which would help to constrain the velocity dependence of the drag. An experimental setup with a more precise launching mechanism and a faster way to resurface the bed would help eliminate unsuccessful trials and reduce the lateral motion and history dependence. However, such effects are interesting in their own right, and may be important to any practical applications of rolling over granular media. In particular, the sideways veering of the cylinders as they leave the centreline of the channel is suggestive of an instability that deserves further exploration.

Acknowledgements: The lab experiments and initial modeling was conducted at the 2016 Geophysical Fluid Dynamics Summer Study Program at the Woods Hole Oceanographic Institution, which is supported by the National Science Foundation and Office of Naval Research. We thank Anders Jensen for assistance with the experiments.

References

1. Bekker MG.
   Introduction to terrain-vehicle systems.
   University of Michigan Press; 1969.
2. Ding L, Gao H, Deng Z, Nagatani K, Yoshida K.
   Experimental study and analysis on driving wheels performance for planetary exploration rovers moving in deformable soil.
   Journal of Terramechanics. 2011;48(1):27–45.
3. Johnson JB, Kulchitsky AV, Duvoy P, Iagnemma K, Senatore C, Arvidson RE, et al.
   Discrete element method simulations of Mars Exploration Rover wheel performance.
   Journal of Terramechanics. 2015;62:31–40.
4. Kirkby M, Statham I.
   Surface stone movement and scree formation.
   The Journal of Geology. 1975;83(3):349–362.
5. Reynolds O.
   On rolling friction.
   Philosophical Transactions of the Royal Society of London. 1876;166:155–174.
6. Eldredge K, Tabor D; The Royal Society.
   The mechanism of rolling friction. I. The plastic range.
   Proceedings of the Royal Society of London A: Mathematical, Physical and Engineering Sciences. 1955;229(1177):181–198.
7. Kendall K.
   Rolling friction and adhesion between smooth solids.
   Wear. 1975;33(2):351–358.
8. Gee-Clough D.
   The effect of wheel width on the rolling resistance of rigid wheels in sand.
   Journal of Terramechanics. 1978;15(4):161–184.
9. Wong JY, Reece A.
   Prediction of rigid wheel performance based on the analysis of soil-wheel stresses part I. Performance of driven rigid wheels.
   Journal of Terramechanics. 1967;4(1):81–98.
10. Wong JY, Reece A.
    Prediction of rigid wheel performance based on the analysis of soil-wheel stresses: Part II. Performance of towed rigid wheels.
    Journal of Terramechanics. 1967;4(2):7–25.
11. Wong JY.
    Behaviour of soil beneath rigid wheels.
    Journal of Agricultural Engineering Research. 1967;12(4):257–269.
12. Wiendieck KW.
    A theoretical evaluation of the shear-to-normal stress ratio at the soil-wheel interface.
    Journal of Terramechanics. 1968;5(4):9–25.

13. Nowatzki E, Karafiath LL.
General yield conditions in a plasticity analysis of soil-wheel interaction.
Journal of Terramechanics. 1974;11(1):29–44.
14. Senatore C, Iagnemma K.
Analysis of stress distributions under lightweight wheeled vehicles.
Journal of Terramechanics. 2014;51:1–17.
15. Hambleton J, Drescher A.
On modeling a rolling wheel in the presence of plastic deformation as a three-or two-dimensional process.
International Journal of Mechanical Sciences. 2009;51(11):846–855.
16. De Blasio FV, Saeter MB.
Rolling friction on a granular medium.
Physical Review E. 2009 Feb;79(2):022301.
17. Andreotti B, Forterre Y, Pouliquen O.
Granular media: between fluid and solid.
Cambridge University Press; 2013.
18. Spencer A.
Perturbation methods in plasticity: I plane strain of non-homogeneous plastic solids.
Journal of the Mechanics and Physics of Solids. 1961;9(4):279–288.
19. Spencer A.
Perturbation methods in plasticity: III plane strain of ideal soils and plastic solids with body forces.
Journal of the Mechanics and Physics of Solids. 1962;10(2):165–177.
20. Marshall EA.
Rolling contact with plastic deformation.
Journal of the Mechanics and Physics of Solids. 1968 Aug;16(4):243–254.
21. Tordesillas A, Shi J.
The frictionless rolling contact of a rigid circular cylinder on a semi-infinite granular material.
Journal of engineering mathematics. 2000;.
22. Terzaghi K.
Theoretical soil mechanics.
Chapman And Hall Limited, London; 1943.
23. Salençon J.
Application of the theory of plasticity in soil mechanics.
John Wiley & Sons.; 1977.
24. Martin C.
Exact bearing capacity calculations using the method of characteristics.
Proc IACMAG Turin. 2005;p. 441–450.
25. Collins I.
Rolling of a rigid cylinder on a rigid-perfectly plastic half-space.
Journal de Mécanique appliquée. 1978;2(4):431–448.
26. Petryk H.
A slip-line field analysis of the rolling contact problem at high loads.
International journal of mechanical sciences. 1983;.
27. Sauret A, Balmforth NJ, Caulfield CP, McElwaine JN.
Bulldozing of granular material.
Journal of Fluid Mechanics. 2014 Jun;748:143–174.
28. Bradski G.
Open Source Computer Vision Library.
Dr Dobb's Journal of Software Tools. 2000;.
29. Poorooshasb H, Holubec I, Sherbourne A.
Yielding and flow of sand in triaxial compression: Parts II and III.
Canadian Geotechnical Journal. 1967;4(4):376–397.
30. Roscoe KH.
The influence of strains in soil mechanics.
Geotechnique. 1970;20(2):129–170.

A. Velocity field and free surface shape

In a generalization of Mohr-Coulomb theory, the characteristics of the velocity field are given by

$$\mathrm{d}z = \tan(\theta - \tfrac{1}{4}\pi - \nu)\mathrm{d}x, \quad \mathrm{d}u + \tan(\theta - \tfrac{1}{4}\pi - \nu)\,\mathrm{d}w = 0, \tag{A 1}$$

and

$$\mathrm{d}z = \tan(\theta + \tfrac{1}{4}\pi + \nu)\mathrm{d}x, \quad \mathrm{d}u + \tan(\theta + \tfrac{1}{4}\pi + \nu)\,\mathrm{d}w = 0, \tag{A 2}$$

where ν is the angle of dilation such that

$$u_x + w_z = -\sin\nu\sqrt{(u_x - w_z)^2 + (u_z + w_x)^2}. \tag{A 3}$$

(*e.g.* [29,30]). Only when $\nu = \phi$ (the traditional Mohr-Coulomb model) do the characteristics of the stress and velocity fields coincide.

To construct the velocity field associated with our leading-order stress field solution, we integrate (A 1) and (A 2) numerically using centred differences on a grid defined by the characteristics of the velocity field, exploiting the self-similar solution for θ. We begin the integration along the lowest $\alpha-$line within the yielded region and the $\beta-$line forming the yielded edge of the rotating plug. If these curves are not velocity characteristics ($\nu \neq \phi$) the velocity must be prescribed on both borders in order to match with the stationary unyielded material below and the rigidly rotating plug to the back. If $\nu = \phi$, the two borders are velocity characteristics and slip is allowed along them, implying that only the normal velocity components is prescribed. The numerical integration then progresses upward and rightward to furnish the velocity field over the characteristic web underneath the last velocity characteristic leaving the top right corner of the rotating plug. Above this curve, the characteristics no longer begin from the plug, but from the yielded section of the $x-$axis. There, the $z = 0$ intercepts of the upcoming characteristics must be found, and new downgoing characteristics then launched to complete the web throughout the yielded region, taking the prescribed normal velocity $w = -\Omega(a + x)$ as the boundary condition.

The velocity field computed for the sample solution of figure 8 is shown in figure 13 for $\nu = \phi$ and $\nu = 0$. In the first case, the velocity becomes arbitrarily large at the right-hand edge of the contact region, as for the problem of a critically loaded foundation [24], which reflects the well-known deficiency of the traditional Mohr-Coulomb model in predicting excessive dilation during flow. By contrast, a dilation angle of $\nu = 0$ furnishes an incompressible flow that is free of singularity, and velocity characteristics that no longer coincide with those of the stress, which exposes a stationary, yielded zone underneath the flow region.

Let $z = h = O(a^2/R)$ denote the position of the granular surface. For nearly steady rolling ($\dot{Z} \approx 0$), the back contact point lies at the bottom of the roller and the kinematic condition for the free surface becomes $-\dot{X}h_x = w + O(a^2\dot{X}/R^2)$. Hence,

$$h = \int_x^{x_f} \frac{w}{\dot{X}}\mathrm{d}x = h_b + \frac{a^2}{2R} - \int_0^x \frac{w}{\dot{X}}\mathrm{d}x \quad \text{for} \quad 0 < x < x_f, \tag{A 4}$$

where $h_b = h(-a)$, x_f denotes the front of the bow wave (where $h = 0$), and we have matched to the contact arc below the roller, where $h = h_b + (x + a)^2/(2R)$ for $-a < x < 0$. Note that

$$\int\!\!\int_{\mathcal{A}} (u_x + w_z)\,\mathrm{d}x\mathrm{d}z = \int_0^{x_f} w(x, 0)\,\mathrm{d}x - \tfrac{1}{2}a^2\Omega = \dot{X}h_b, \tag{A 5}$$

where $\mathcal{A}$ denotes the area over which deformation takes place. Thus, without dilation, mass conservation demands that the free surface descends exactly to the bottom of the roller ($h_b = 0$). Conversely, any dilation implies that the incoming granular surface lies below the roller ($h_b > 0$), for which there was no experimental evidence (if anything, the medium compacted and the cylinders rolled at a position below the incoming surface). The predicted free surfaces for the two values of dilation angle are also presented in figure 13. The excessive dilation of the Mohr-Coulomb model with $\nu = \phi$ leads to an unphysical descent of the free surface, which is avoided by taking $\nu = 0$.

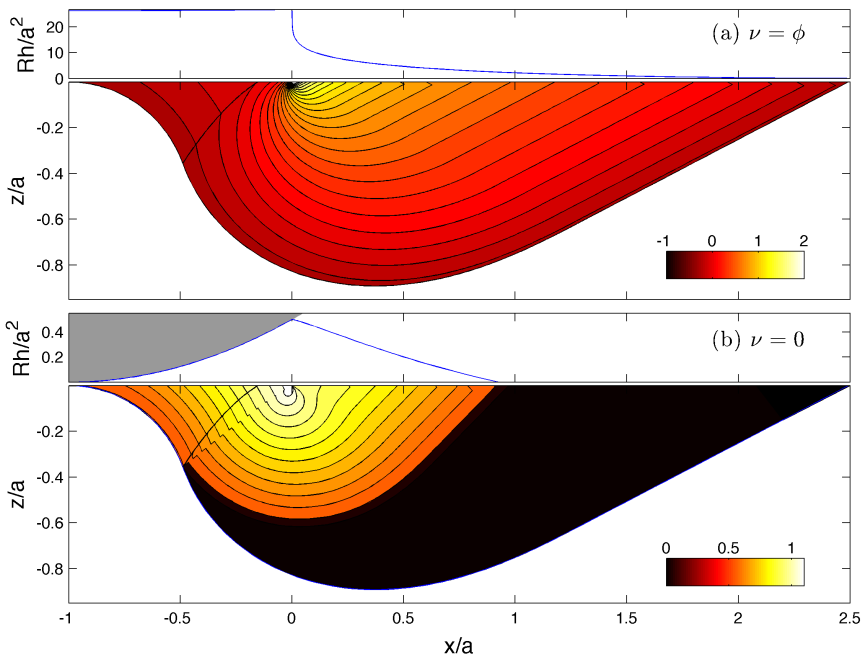

Figure 13: Speed contours for $\phi = 36°$, $\psi_p = -4\pi/5$, $\theta_f = -\frac{1}{2}\varepsilon$, plotting (a) $\log_{10}(\sqrt{u^2+w^2}/a\Omega)$ for $\nu = \phi$, and (b) $\sqrt{u^2+w^2}/a\Omega)$ for $\nu = 0$. For each, the predicted free surface shape is shown above.

B. The Collins solution for $a \ll R$

For cohesive material without gravity, the $p\sin\phi$ factors in (3.9) are replaced by the cohesion c, and the slipline solution consists of a Rankine wedge leading a centred fan with circular $\alpha-$lines and straight radial $\beta-$lines. The fan geometry demands that the $\beta-$lines be straight everywhere, and so the rigidly rotating plug attached to the roller spans the entire footing and $\ell = \tan\psi_p$; see figure 14. Within the Rankine wedge the sliplines are inclined at $\pm\frac{1}{4}\pi$ to the horizontal, with $\theta = \frac{1}{2}\pi$ and $p = c$ ($\epsilon \equiv \frac{1}{4}\pi$). The fan extends back to the angle ψ_p from $\psi = -\frac{1}{4}\pi$, and within it, $\theta = \frac{3}{4}\pi + \psi$ and $p + 2c\theta = c(1+\pi)$, or $p = c(1 - \frac{1}{2}\pi - 2\psi)$. Along the circular failure arc that continues the lowest $\alpha-$line, $\theta = \frac{1}{4}\pi - \chi$ and $p + 2c\theta = c(1+\pi)$, or $p = c(1 + \frac{1}{2}\pi + 2\chi)$, for $0 \le \chi \le -\psi_p - \frac{1}{2}\pi$. The force exerted on the roller can then be determined by integrating over the contour $\mathcal{L}$ as in §3. Again, there is a special value, $\ell = \ell_* \approx 0.43$, for which the horizontal force vanishes, leading to the lift force, $F_z \sim 4.90ac$, and rolling resistance, $F_r \sim 3.25a^2c/R$.

Within the yielded region, the velocity field is directed along the $\alpha-$lines with speed $u_\alpha = -\Omega(r + a\sec\psi_p)$ (the velocity equations are $\mathrm{d}u_\alpha = -u_\beta \mathrm{d}\theta$ and $\mathrm{d}u_\beta = u_\alpha \mathrm{d}\theta$ along the two characteristics, and $u_\beta = 0$ along the lowest $\alpha-$line, implying $u_\beta = 0$ everywhere); *cf.* figure 14(b). The velocity at the free surface is therefore $\frac{1}{2}\sqrt{2}u_\alpha(1,1) = -\frac{1}{2}\Omega(x + a\sqrt{2}\sec\psi_p)(1,1)$, which implies the free surface profile from (A 4),

$$h(x) = \frac{a^2}{2R} + \frac{x}{4R}(x + 2a\sqrt{2}\sec\psi_p). \tag{A 1}$$

At the front of the bow wave, $x = x_f \equiv -a(\sec\psi_p + \tan\psi_p)\sqrt{2}$, we find $h = 0$, confirming that the bottom of the roller lies at the level of the undeformed surface; see figure 14.

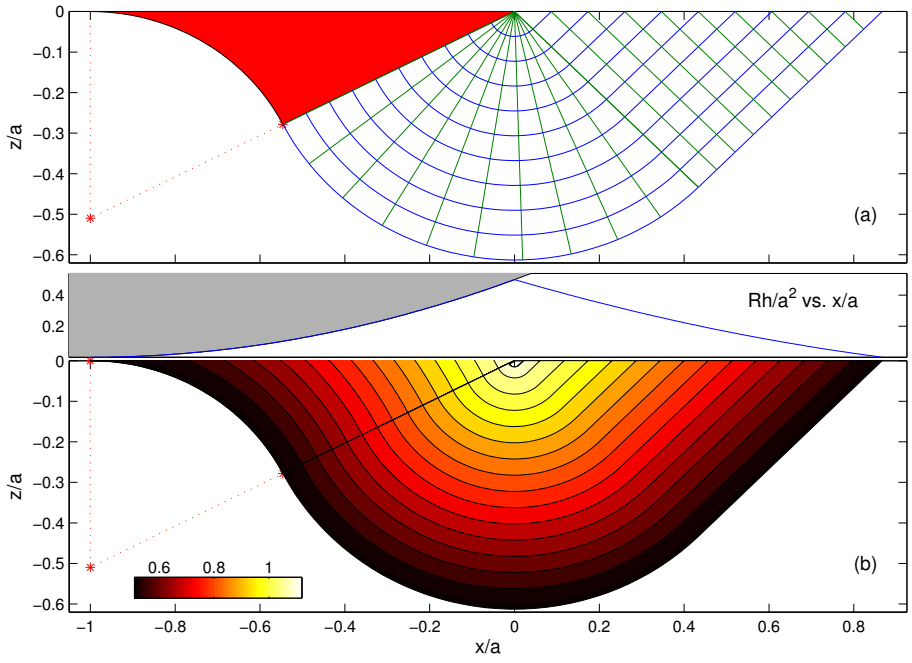

Figure 14: (a) Slipline field and (b) speed contours of the cohesive solution for $\psi_p = -17\pi/20$. The scaled free-surface shape $Rh(x)/a^2$ is also plotted in (b).